Eur. Phys. J. E (2013) **36**: 139
DOI 10.1140/epje/i2013-13139-3

THE EUROPEAN PHYSICAL JOURNAL E

Regular Article

On the determination of a generalized Darcy equation for yield-stress fluid in porous media using a Lattice-Boltzmann TRT scheme

Laurent Talon[1,a] and Daniela Bauer[2]

[1] Univ. Pierre et Marie Curie-Paris6, Univ. Paris-Sud, CNRS, Lab. FAST, Bât. 502, Campus Univ., Orsay, F-91405, France
[2] IFP Energies nouvelles, 92852 Rueil-Malmaison, France

Received 5 June 2013 and Received in final form 23 October 2013
Published online: 11 December 2013 – © EDP Sciences / Società Italiana di Fisica / Springer-Verlag 2013

Abstract. Simulating flow of a Bingham fluid in porous media still remains a challenging task as the yield stress may significantly alter the numerical stability and precision. We present a Lattice-Boltzmann TRT scheme that allows the resolution of this type of flow in stochastically reconstructed porous media. LB methods have an intrinsic error associated to the boundary conditions. Depending on the schemes this error might be directly linked to the effective viscosity. As for non-Newtonian fluids viscosity varies in space the error becomes inhomogeneous and very important. In contrast to that, the TRT scheme does not present this deficiency and is therefore adequate to be used for simulations of non-Newtonian fluid flow. We simulated Bingham fluid flow in porous media and determined a generalized Darcy equation depending on the yield stress, the effective viscosity, the pressure drop and a characteristic length of the porous medium. By evaluating the flow in the porous structure, we distinguished three different scaling regimes. Regime I corresponds to the situation where fluid is flowing in only one channel. Here, the relation between flow rate and pressure drop is given by the non-Newtonian Poiseuille law. During Regime II an increase in pressure triggers the opening of new paths and the relation between flow rate and the difference in pressure to the critical yield pressure becomes quadratic: $q \propto (\tilde{dp} - \tilde{dp}_c)^2$. Finally, Regime III corresponds to the situation where all the fluid is flowing. In this case, $q \propto (\tilde{dp} - \tilde{dp}_c)$.

1 Introduction

Non-Newtonian fluids have practical applications in very different domains. Indeed, polymer mixture, paints, slurries, colloidal suspensions, emulsions, foams or heavy oil present complex rheologies. Among the large number of different non-Newtonian fluids an important class of behavior is represented by the yield-stress fluids, viz. fluids that require a minimum of stress to flow. Yield-stress fluids are usually modelled as a Bingham fluid or by the Herschel-Bulkley equation. Yield-stress fluid displacements in porous media have been subject of particular interest due to the yield-stress behavior of heavy oil [1] or foam [2].

In the literature, most of the numerical modelling has been made by means of the so-called "pore network" approach [2–9]. Pore network modelling is based on a simplified representation of the pore space by a three-dimensional network of interconnected pores and throats. In each throat, a relationship between flow rate and pressure difference is assumed (similarly to the current-voltage relationship in a network of resistances [3]). This method has the main advantage to be efficient as it only requires the resolution of a simplified equation in each throat. However, the flow rate expression of a yield-stress fluid is a complex nonlinear function of the pressure gradient (see for instance eq. (11) for the uniform 2D Poiseuille flow). To overcome this difficulty, the different approaches assumed then a simplified flow rate relationship (linear, quadratic, etc.). Except for the work of Balhoff and Thompson [5] the throat geometry is usually assumed to be uniform which could affect the effective pressure threshold. Due to this simplification the different attempts to compare the numerical model to the experimental data [10–13] were not entirely satisfactory (see [5,7,8]). Additionally, the presence of a yield stress seems to alter significantly the stability and the precision of the numerical modelling [9]. This is illustrated by the fact that pore network modelling correctly reproduces the behavior of non-Newtonian fluids without yield stress but incorrectly the behavior of yield-stress fluids (see [7] for the two cases).

In the present article, we will present a numerical method that can handle these difficulties. The method is based on a Lattice Boltzmann scheme [14–19] that allows the resolution of the (Navier-)Stokes equation at the pore scale in complex structures. Lattice-Boltzmann

[a] e-mail: talon@fast.u-psud.fr

methods have been successfully applied to solve flow of non-Newtonian fluids without yield stress (see [20–22]). Yet, the presence of a threshold in the stress induces numerical errors and instabilities. This is due to the fact that it is necessary to define an effective viscosity that diverges for small shear. One possibility to cope with this problem has been introduced by Vikhansky [23] and it is based on an implicit Lattice-Boltzmann scheme. In the present article, we will follow the work of [24] who suggested a multiple-relaxation-time scheme (MRT) to simulate Bingham fluids.

From a physical point of view, as demonstrated using the "pore-network model" approach by [3], the flow rate curve might display different scaling regimes with the pressure depending on the rheological parameters and the structure of the medium. These regimes are characterized by a power law whose exponent depends on the amount of fluid that is flowing. The exponent is one when the fluid is flowing in either only one chanel or in the entire domain. An intermediate regime, with an exponent of two, characterizes the regime where the amount of flowing fluid increases with the applied pressure. One should also mention that in a recent paper, Sinha and Hansen [25] have predicted this quadratic dependence with a mean field approach.

The objective of this article is then mainly twofold. First, we will present a numerical scheme able to solve Bingham fluid displacement in a stochastically reconstructed porous media. Secondly, we will determine a generalized Darcy equation and investigate the different flow regimes induced by the yield stress and the heterogeneities of the media.

2 Equation of flow — Numerical Implementation

2.1 Bingham fluid

The momentum equation defining Stokes flow is given by

$$\mathbf{0} = -\boldsymbol{\nabla} P + \boldsymbol{\nabla} \cdot \boldsymbol{\Pi}, \tag{1}$$

where $\boldsymbol{\Pi}$ is the shear stress tensor and P the pressure.

For a Bingham fluid, the shear stress follows

$$\boldsymbol{\Pi}_{ij} = 2\rho\nu_0 \left(1 + \frac{\tau_0}{2\dot{\gamma}\rho\nu_0}\right) \boldsymbol{\Delta}_{ij}, \tag{2}$$

where

$$\boldsymbol{\Delta}_{ij} = \frac{1}{2}\left(\frac{\partial \boldsymbol{u}_i}{\partial x_j} + \frac{\partial \boldsymbol{u}_j}{\partial x_i}\right)$$

is the deformation rate tensor and $\dot{\gamma} = \sqrt{2\boldsymbol{\Delta}_{ij}\boldsymbol{\Delta}_{ij}}$ is the shear rate. $\boldsymbol{u}$ is the velocity field, τ_0 is the yield stress, ν_0 the kinematic Bingham viscosity and ρ the density.

An effective kinematic viscosity can thus be determined by

$$\nu_{\text{eff}}(\dot{\gamma}) = \nu_0 + \frac{\tau_0}{\rho\dot{\gamma}}\,. \tag{3}$$

For very low shear rates, the effective viscosity diverges to infinity. However, in order to overcome this restriction numerically, we use the classical regularized viscosity function as in [26,24]

$$\nu_{\text{eff}}(\dot{\gamma}) = \nu_0 + \frac{\tau_0}{\rho\dot{\gamma}}(1 - e^{-m\dot{\gamma}}), \tag{4}$$

where m is a regularization coefficient.

It is important to note that the main consequence of such regularized function is the fact that now the viscosity tends to a finite (large) value for low shear. Indeed, we have

$$\lim_{\dot{\gamma}\to 0} \nu_{\text{eff}}(\dot{\gamma}) = \nu_0 + \frac{\tau_0 m}{\rho}\,. \tag{5}$$

Thus, in the numerical simulations, the fluid is not strictly "solid" but only extremely viscous. In that case, its viscosity is mostly characterized by m.

2.2 Poiseuille flow

The velocity profile of a Bingham fluid driven by a (negative) pressure gradient in a two-dimensional configuration can be easily computed. Naming x and y the gap-wise and stream-wise direction respectively, eq. (1) becomes

$$\frac{\partial P}{\partial x} = \frac{\partial}{\partial y}\Pi_{xy}. \tag{6}$$

By symmetry, the shear stress is nil in the centre. Thus, after integration, eq. (6) leads to

$$\Pi_{xy} = y\partial_x P. \tag{7}$$

Equation (2) can be written as

$$\frac{\partial u_x}{\partial y} = 0, \quad \text{if } |\Pi_{xy}| < \tau_0, \tag{8}$$
$$\frac{\partial u_x}{\partial y} = \frac{1}{\rho\nu_0}(\Pi_{xy} - \text{sign}(\Pi_{xy})\tau_0), \quad \text{if } |\Pi_{xy}| > \tau_0.$$

Combining, eqs. (7) and (8) and assuming a negative pressure gradient ($\partial_x P < 0$), the velocity field becomes

$$u_x(y) = U_0, \quad \text{for } |y| < b\left|\frac{\tau_0}{\tau_w}\right|, \tag{9}$$
$$u_x(y) = U_0 - \frac{1}{2\rho\nu_0}\frac{\tau_w}{b}\left(|y| - b\frac{\tau_0}{\tau_w}\right)^2, \quad \text{for } |y| > b\left|\frac{\tau_0}{\tau_w}\right|,$$

where $2b$ is the width of the channel. The shear at the wall is given by $\tau_w = -b\,\partial_x P > 0$ and

$$U_0 = \frac{1}{2\rho\nu_0} b\tau_w \left(1 - \frac{\tau_0}{\tau_w}\right)^2. \tag{10}$$

By integration, the flow rate is determined as a function of the pressure gradient

$$Q_{\text{th}} = \frac{2b^3}{3\rho\nu_0}\left(\frac{1}{\partial_x P}\right)^2 \left(\partial_x P - \frac{\tau_0}{b}\right)^2 \left(\partial_x P + \frac{\tau_0}{2b}\right). \tag{11}$$

It is important to note that the flow condition is given by the non-dimensional number $\tau_0/\tau_w = \tau_0/b\partial_x P$ which compares the stress at the wall to the yield stress. This quantity gives also the size ratio of the solid region to the flowing one (see eq. (9)).

2.3 TRT scheme

In this section, we will briefly describe the numerical scheme used to solve the flow equation (for further details see [24,27–29,19]).

As a matter of principle, the basic idea of the Lattice-Boltzmann method is to discretize the velocity distribution function of particles on a grid. To this goal, we introduce the population f_q as the density of particles moving with the velocity $\boldsymbol{c}_q$. The algorithm is mainly a succession of two steps. The first is the propagation step (eq. (12)), where we move the density on the grid according to its velocity. The second is the collision step (eq. (13)), where we redistribute populations meeting at the same node using a collision operator that depends on the local macroscopic quantities (pressure, velocity, etc.).

We used here a two-dimensional equation with a nine population distribution (D2Q9) scheme. The nodes of the grid are related by the velocity vectors $\boldsymbol{c}_q$, $q = 1, \ldots, 9$ and $\boldsymbol{c}_0 \equiv \boldsymbol{0}$. We assume that the first 4 vectors $\boldsymbol{c}_q$ are opposite to the second set of 4 vectors defined as $\boldsymbol{c}_{\bar{q}} = -\boldsymbol{c}_q$. We then operate with the symmetric $\{f_q^+ = (f_q + f_{\bar{q}})/2\}$ and the anti-symmetric $\{f_q^- = (f_q - f_{\bar{q}})/2\}$ components, $q = 1, \ldots, 4$. We set $f_0^+ = f_0$ and $f_0^- = 0$ for immobile population. The two-relaxation-times (TRT) update is performed with the prescribed equilibrium distribution $\{e_q^\pm\}$ and two collision eigenvalues $s^\pm \in]0, 2[$, s^+ for all symmetric and s^- for all anti-symmetric non-equilibrium components, $\{n_q^+\}$ and $\{n_q^-\}$, respectively. Thus, we obtain

$$\begin{aligned} f_0(\boldsymbol{r}, t+1) &= [f_0(1-s^+) + s^+ e_0](\boldsymbol{r}, t), \\ f_q(\boldsymbol{r} + \boldsymbol{c}_q, t+1) &= \tilde{f}_q(\boldsymbol{r}, t), \end{aligned} \tag{12}$$

with

$$\begin{aligned} \tilde{f}_q(\boldsymbol{r}, t) &= [f_q - s^+ n_q^+ - s^- n_q^-](\boldsymbol{r}, t)\,,\ q = 1, \ldots, 4, \\ \tilde{f}_{\bar{q}}(\boldsymbol{r}, t) &= [f_{\bar{q}} - s^+ n_q^+ + s^- n_q^-](\boldsymbol{r}, t)\,,\ q = 1, \ldots, 4\,, \end{aligned} \tag{13}$$

where

$$n_q^\pm = (f_q^\pm - e_q^\pm)\,, \quad \text{when } \boldsymbol{c}_{\bar{q}} = -\boldsymbol{c}_q\,,\ q = 1, \ldots, 4. \tag{14}$$

Computing the linear collision operator we have accounted that the symmetric components are the same for two opposite populations, and hence $f_q^+ = f_{\bar{q}}^+$, $n_q^+ = n_{\bar{q}}^+$, while the anti-symmetric components have the opposite signs, and hence $f_q^- = -f_{\bar{q}}^-$, $n_q^- = -n_{\bar{q}}^-$.

The fluid dynamics are obtained by prescribing the equilibrium functions $e_q^\pm$. The latter require the computation of two quantities: the local mass

$$\rho = \sum_{q=0}^{9} f_q = f_0 + 2\sum_{q=1}^{4} f_q^+, \tag{15}$$

and local momentum

$$\boldsymbol{j} = \sum_{q=1}^{9} f_q \boldsymbol{c}_q = 2\sum_{q=1}^{4} f_q^- \boldsymbol{c}_q. \tag{16}$$

Equilibrium functions then become

$$e_q^+ = c_s^2 t_q^\star \rho\,, \quad e_q^- = t_q^\star (\boldsymbol{j} \cdot \boldsymbol{c}_q)\,, \quad e_0 = \rho - 2\sum_{q=1}^{4} e_q^+, \tag{17}$$

where the weights $\{t_q^\star\}$ take the value $t_q^\star = \{t^{\mathrm{I}}, t^{\mathrm{II}}\} = \{\frac{1}{3}, \frac{1}{9}\}$ for respectively the first and second (diagonal) neighbour link in the D2Q9 model.

This TRT scheme models solutions to Stokes equations (in lattice units) by

$$\partial_t \rho + \boldsymbol{\nabla} \cdot \boldsymbol{j} = 0\,, \quad \partial_t \boldsymbol{j} + \boldsymbol{\nabla} P = \nu_{\text{eff}} \Delta \boldsymbol{j}, \tag{18}$$

where the kinematic viscosity is given by $\nu_{\text{eff}} = \frac{1}{3}(\frac{1}{s^+} - \frac{1}{2})$, the pressure P by $P = c_s^2 \rho$ and the macroscopic momentum by $\boldsymbol{u} = \boldsymbol{j}/\rho_0$, where ρ_0 is a constant and taken as the initial mass average of the fluid (routinely, ρ_0 equals 1). The sound velocity c_s is set to $\sqrt{\frac{1}{3}}$. In the TRT scheme, the second eigenvalue s^- is a free parameter (we recall that $s^- \in]0, 2[$).

As discussed in detail in [28,30,19], LBM methods (BGK, MRT,...) may have an intrinsic error associated to the bounce-back boundary condition. This error is linked to the viscosity parameter ν, as long as the relation between the odd and even relaxation parameter $\Lambda = (\frac{1}{s^+} - \frac{1}{2})(\frac{1}{s^-} - \frac{1}{2})$ is not kept constant. For Newtonian fluids, this error leads to a dependence of the permeability with the viscosity (see also [31]) whereas in the TRT scheme $\nu \boldsymbol{j}$ is strictly independent of ν, as it should for Stokes flow.

For non-Newtonian fluids, this effect is even more drastic as the effective viscosity strongly varies in space (see below), making the error inhomogeneous. Additionally, we report that there is a stability problem with the standard BGK scheme. For that reason, we will hereafter use Λ as control parameter rather than s^-.

To simulate non-Newtonian fluid flow one needs to introduce an effective viscosity ν_{eff} that varies with the local shear rate $\dot{\gamma}$. An interesting feature of the LBE scheme is the fact that the local deformation rate tensor is simply obtained from the non-equilibrium distribution (see [24])

$$\begin{aligned} \Delta_{ij} &= \frac{1}{2\rho_0}(\boldsymbol{\nabla} \boldsymbol{j} + (\boldsymbol{\nabla} \boldsymbol{j})^T) \\ &= -s^+ \frac{3}{2\rho_0} \sum_{1}^{9} n_q^+ c_{qi} c_{qj} \\ &= -s^+ \frac{3}{\rho_0} \sum_{1}^{4} n_q^+ c_{qi} c_{qj}. \end{aligned} \tag{19}$$

The algorithm is implemented as follows. Initially, the fluid has a homogeneous effective viscosity ν_{eff}. We apply a pressure drop ΔP between the inlet and outlet. At each time step, the local shear rate is computed using eq. (19) to update the local effective viscosity using eq. (4). The iteration is pursued until convergence of the flow field is reached (which typically takes around 10^5-10^9 time steps).

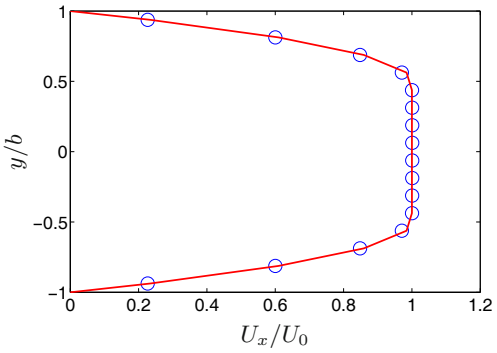

Fig. 1. Numerical velocity field (normalized by the theoretical velocity at the centre U_0) inside a two-dimensional chanel compared to the theoretical prediction (eq. (9)). The numerical parameters are $b = 8\ \delta x, m = 10^9, \Lambda = 0.2, \nu_0 = 0.001$, $\tau_0 = 10^{-5}$, $\tau_0/\tau_w = 0.5$.

For the lattice-Boltzmann scheme, typically used values are $\Lambda = 0.2$, $\nu_0 = 10^{-3}$, $\tau_0/\rho \simeq 10^{-5}$ and $m = 10^9$, which allow to have several orders of magnitude between the viscosity of the "solid" and the fluid. In the following, units of the presented quantities are expressed in terms of the lattice grid unit and iteration time step.

The correspondance between the numerical and experimental data requires the determination of a characteristic length ($l^* = \lambda$, b or $\sqrt{K}$), a characteristic pressure $p^* = \tau_0$ and a characteristic velocity $v^* = l^* p^*/\rho\nu_0$ (based on the dynamic viscosity). The correspondance for any distance, pressure or velocity are then obtained by

$$x_{\rm exp} = \frac{l^*_{\rm exp}}{l^*_{\rm num}} x_{\rm num}, \tag{20}$$

$$P_{\rm exp} = \frac{p^*_{\rm exp}}{p^*_{\rm num}} P_{\rm num}, \tag{21}$$

$$q_{\rm exp} = \frac{v^*_{\rm exp}}{v^*_{\rm num}} q_{\rm num}. \tag{22}$$

2.4 Validation

In order to validate the scheme, we will present the results of the flow simulation performed in a Poiseuille configuration as described in sect. 2.2. Figure 1 displays the theoretical velocity profile as well as the numerical one. The following parameters were used: $b = 8$, $\nu_0 = 10^{-3}$, $m = 10^9$, $\Lambda = 0.2$ and $\tau_0/\tau_w = 0.5$. We remark here that despite the coarse grid used (given by the points in the figure), the numerical profile is in good accordance with the theoretical prediction. Moreover, it is also important to compare the flow for different size ratio of the sheared and unsheared regions. Figure 2 (left) displays the flow rate Q normalized by the theoretical one (eq. (11)) as a function of the unsheared width $b\tau_0/\tau_w$. We can see a good agreement for $b\tau_0/\tau_w < 6$. However, a significant discrepancy can be observed, when the unsheared zone reaches the wall. As it can be seen in fig. 2 (right), the discrepancy is relative and due to the fact that the theoretical flow rate tends to zero (see eq. (10)) wheras the numerical one can not as the numerical viscosity tends not to infinity but to a large finite value. It should be noted that this discrepancy can be reduced by increasing the numerical value m. However, for too high values of m, numerical instabilities have been observed. Moreover, on this figure, we show that $\nu_0 Q$ is independent of the numerical parameter ν_0.

Figure 3 displays the relative error of the flow rate *vis à vis* of the discretization b. As expected, the numerical results become more accurate when the number of grid points is increased.

Finally, we evaluated the influence of Λ on the velocity profile. To this goal, Λ was varied in the intervall $\Lambda \in [0.1, 0.4]$ with the resolution $b = 4$. We found a maximal error of $Q/Q_{\rm th}$ of 2%. Thus, the influence of the value of Λ on the results of the present simulations is negligible.

2.5 Porous media generation

We used the spectral method proposed in [19,32] to generate the porous medium. To this goal, we first generate a matrix $W(\boldsymbol{r})$ of white random noise. After multiplying its Fourier transform ($Z(\boldsymbol{r})$) with a Gaussian function we obtain:

$$Z'(\boldsymbol{k}) = \alpha Z(\boldsymbol{k}) e^{-\frac{|\boldsymbol{k}|^2}{k_0^2}}. \tag{23}$$

A fast inverse Fourier transform $f(\boldsymbol{r}) = FT^{-1}(Z'(\boldsymbol{k}))$ leads then to a Gaussian distributed noise correlated with a Gaussian correlation function

$$FT(f \cdot f^*) = \alpha^2 e^{-2\frac{|\boldsymbol{k}|^2}{k_0^2}}.$$

This leads to the autocorrelation function

$$f * f(x) \propto e^{-\frac{k_0^2}{8}|r|^2} = e^{-\frac{1}{2}\left(\frac{\pi|r|}{2\lambda}\right)^2}, \tag{24}$$

where $\lambda_s = \pi/k_0$. The prefactor α is set, without loss in generality, to have a standard deviation equal to one. The solid lattices are then deduced by a level-set with a given value, f_0: $S = \{\boldsymbol{r} | f(\boldsymbol{r}) < f_0\}$. The porosity ϕ is related to the cumulative distribution function, $P(f)$, which is by construction an error function centered around 0 with a standard deviation of 1

$$f_0 = P^{-1}(\phi).$$

We note that this method is not restricted to $2D$ and has also the advantage of generating periodic media which allow to apply periodic lateral boundary conditions.

The porous media is then characterized by its size ($L_x \times L_x$), correlation length (λ) and porosity (ϕ). A pressure drop ΔP is then applied to the boundaries in order to drive the fluid. After a transient time (between 10^6 and $10^9 \delta t$), a steady velocity field $u(\boldsymbol{r})$ is reached, from which we compute the volume average flow rate

$$q = \frac{1}{V} \int u(\boldsymbol{r}) \mathrm{d}\boldsymbol{r}. \tag{25}$$

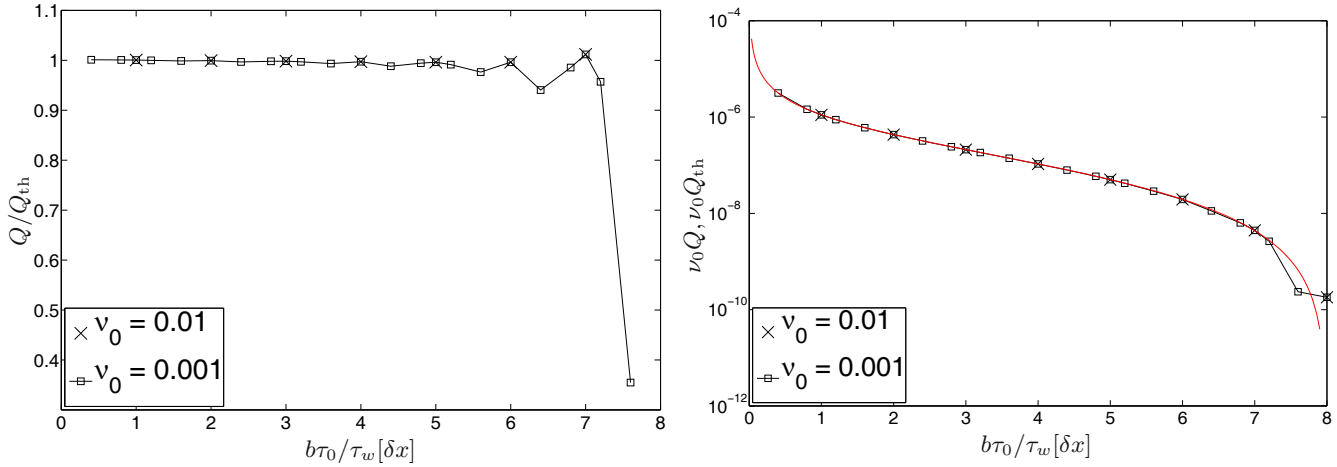

Fig. 2. Left: numerical flow rate Q normalized by the theoretical flowrate $Q_{\rm th}$ as a function of the unsheared width for two different viscosities. Right: numerical flow rate (symbols) and theoretical (line) multiplied by ν_0 as a function of the unsheared width $b\tau_0/\tau_w$. The parameters are the same as in fig. 1.

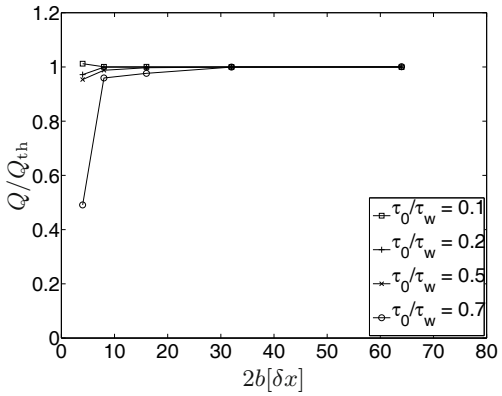

Fig. 3. Relative error for the flow rate $Q/Q_{\rm th}$ as function of the grid width $2b$ for different unsheared width ratio τ_0/τ_w. The parameters are the same as in fig. 1.

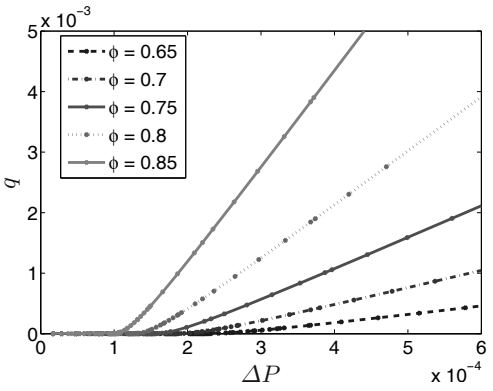

Fig. 4. Average flow rate q as a function of the applied pressure drop ΔP for different porosities. For each random generation, the same seed has been used. The statistical properties are then similar. The numerical parameters are $L_x = 512\ \delta x$, $\lambda = 6\ \delta x$, $m = 10^9$, $\Lambda = 0.2$ and $\nu_0 = 10^{-3}$.

3 Results and discussion

3.1 Flow rate curve

In this section we investigate the dependence of the average flow rate q on the characteristics of the porous medium, the yield stress and the pressure drop in order to determine a generalized Darcy equation.

Figure 4 displays the average flow rate q as a function of the applied pressure drop ΔP for a given value of the yield $\tau_0 = 10^{-6}$ and different porosities. The trend is quite similar for all porosities. It can be seen that a minimal pressure drop ΔP_c is required for the fluid to flow. Beyond this threshold, the flow rate seems to increase linearly with the applied pressure. This trend is qualitatively in agreement with the experimental and numerical works of [10,11,13], where it has been proposed that the flow rate behaves like

$$q \propto k/\mu_{\rm eff}(\boldsymbol{\nabla} P - \boldsymbol{\nabla} P_c)^n, \qquad (26)$$

where n is the Herschel-Bulkley exponent and k the Newtonian permeability. In particular, for Bingham fluids ($n = 1$), this law predicts that at high pressure drop, one should obtain Darcy's law, explaining the fact that the slope increases with the porosity. We also note that porosity is affecting the pressure threshold.

On fig. 5, different velocity fields are represented as a function of the pressure drop ΔP. Close to the threshold ΔP_c fluid is flowing in only few paths. For a pressure difference higher by several orders of magnitude, one can clearly observe that all the fluid in the medium is now flowing, corresponding to Darcy's regime.

Figure 6 (left) displays the flow curves as a function of the pressure drop for different values of the yield stress τ_0 (including the Newtonian case $\tau_0 = 0$) and a given porosity $\phi = 0.75$. As expected, for large enough pressure drop, all curves collapse on the Newtonian one, given by the standard Darcy's law. The threshold pressure is

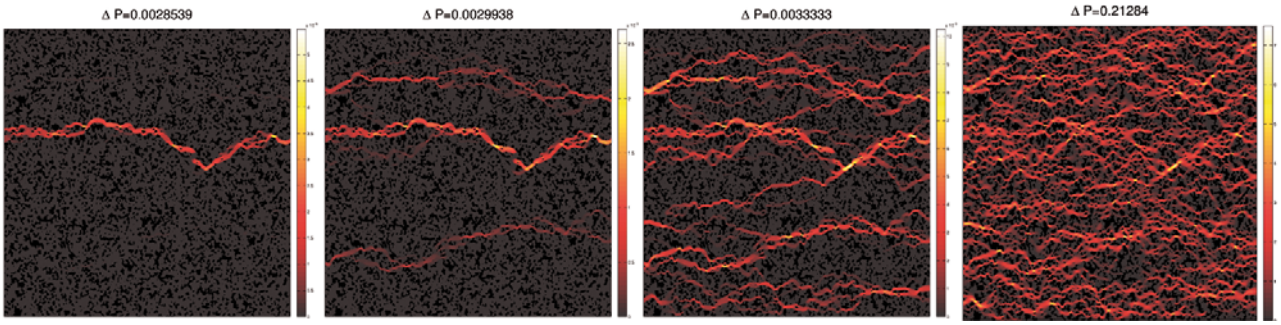

Fig. 5. Flow field example inside the porous media (solid sites are darker) for different applied pressure drop ΔP. The numerical parameters are $\phi = 0.75$, $L_x = 1024\ \delta x$, $\lambda = 6\ \delta x$, $m = 10^9$, $\Lambda = 0.2$, $\nu_0 = 10^{-3}$ and $\tau_0 = 10^{-5}$.

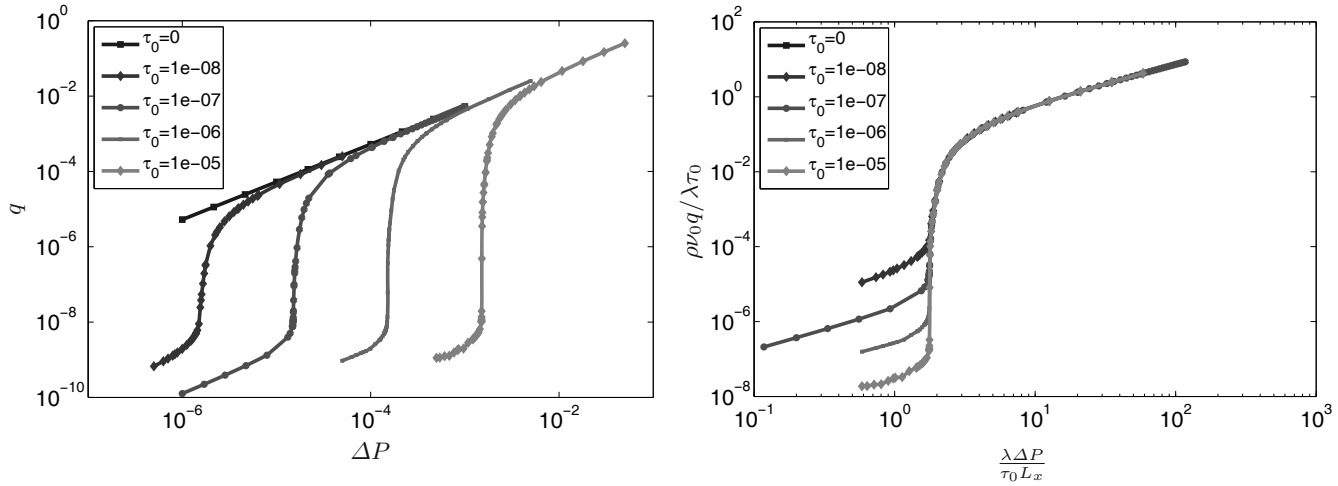

Fig. 6. Left: average flow rate q as a function of the applied pressure drop ΔP for different yield stress τ_0 plotted on a log-log scale as a function of the pressure drop. Right: dimensionless flow rate $\rho\nu_0 * q/\lambda\tau_0$ as a function of the dimensionless parameter $\tilde{dp} = \lambda\Delta P/(\tau_0 L_x)$.

characterized by the large increase of q (depending on τ_0). It is important at this point to underline that below the threshold the flow rate is not strictly zero as expected. This effect is of course a numerical artefact due to the fact that the fluid is never really sheared but has a very large viscosity (of the order of $m\tau_0/\rho$). We also note that in this regime, the relationship between flow and pressure drop is linear, which can be understood as being a Darcy's law with high viscosity.

In order to determine the dependence of q on the characteristic dimensions of the porous medium, we first non-dimensionalize the pressure-flow rate curve. Indeed, from the result of the channel flow (sect. 2.2), it is natural to compare the pressure gradient to the yield stress and the caracteristic length λ. We thus introduce the dimensionaless parameter

$$\tilde{dp} = \frac{\lambda \Delta P}{\tau_0 L_x}\,. \tag{27}$$

We have plotted on fig. 6 (right), the dimensionless flow rate $\tilde{dq} = \rho\nu_0 q/\lambda\tau_0$ as a function of $\tilde{dp}$. As can be seen all curves collapse in the flowing region. Consequently, the flow rate can be written as a function of $\tilde{dp}$, it becomes

$$q = \frac{\lambda\tau_0}{\rho\nu_0}\mathcal{F}\left(\frac{\lambda\Delta P}{\tau_0 L_x}\right). \tag{28}$$

The reason why the flow rate is proportional to $\lambda\tau_0$ can be explained as follows. Indeed, expecting the flow behaving as a Newtonian fluid for very large pressure drop implies that

$$\lim_{\tilde{dp}\to+\infty} \mathcal{F}(\tilde{dp}) \propto \tilde{dp}.$$

In this limit, one should retrieve the standard Darcy's law, which is independent of τ_0 and proportional to the square of the characteristic length λ ($K_{\mathrm{Darcy}} \propto \lambda^2$). We thus have:

$$\lim_{\tilde{dp}\to+\infty} q = \frac{K_{\mathrm{Darcy}}\Delta P}{\rho\nu_0 L_x} = \frac{K_{\mathrm{Darcy}}\tau_0}{\lambda\rho\nu_0}\tilde{dp} \propto \tau_0\lambda^2\tilde{dp}.$$

We note also that the inverse of our dimensionless flow rate could also define a Bingham number $Bi^{-1} = \tilde{dq}$ (based on the volume averaged velocity and the correlation length λ).

Taking into account the pressure threshold, one can then write the flow rate curve in the following form:

$$q = \frac{K_{\mathrm{Darcy}}\tau_0}{\lambda\rho\nu_0}\mathcal{H}\left(\frac{\lambda\Delta P}{\tau_0 L_x} - \tilde{dp}_c\right), \quad (29)$$

$$\text{with} \quad \lim_{x\to\infty}\mathcal{H}(x) = x + O(x).$$

3.2 Pressure threshold-critical length

In order to finalize the generalized Darcy equation (eq. (29)), we determine in the next step the critical pressure threshold $\tilde{dp}_c$ and relate it to a critical length λ_c, a geometrical characteristic of the generated porous medium.

Different methods to determine the critical pressure threshold exist. Unfortunately, none of them is exact and they imply some errors. The easiest method one could imagine is to decrease the flow rate or the applied pressure until the flow is stopped. This method is however difficult to achieve experimentally and numerically. Indeed, experimental set-ups are usually bond to a minimal flow rate or pressure that limits the range in which the flow rate-pressure curve can be determined (see [33] for instance). In the present numerical case, the difficulty results from the fact that the flow rate never drops to zero, due to the finite viscosity constraint. The most commonly used method is then to fit the flow rate-pressure curve and interpolate it to the zero flow rate. The main disadvantage is then that one needs to assume a general form of the curve such as eq. (26). Here, we benefit from the fact that we know the velocity field to determine when the velocity increases significantly in the media.

For routine determination of $\tilde{dp}_c$, the most precise way is based on the fact that, when the fluid is entirely "solid", it has a fixed known viscosity $\nu_0 + \tau_0 m/\rho$. Thus, in the "non-flowing" regime, since the flow behaves as a Newtonian fluid, the quantity $\nu\boldsymbol{u}(\boldsymbol{r})/\nabla P$ is independent of the pressure gradient. Therefore, we first evaluate in the Newtonian case the quantity:

$$\omega_{\max}^{\mathrm{Newt}} = \max_{\boldsymbol{r}}\left(\frac{\nu_0 u(\boldsymbol{r})}{\nabla P}\right).$$

We can then estimate the flowing region by determining at which pressure

$$\frac{u(\boldsymbol{r})}{\nabla P} > 1.1\frac{1}{\nu_0 + \tau_0 m/\rho}\omega_{\max}^{\mathrm{Newt}}.$$

The coefficient 1.1 is an *ad hoc* coefficient. One can also quantify the averaged flowing regions by:

$$\mathcal{O}(\tilde{dp}_c) = \left\langle \frac{u(\boldsymbol{r})}{\nabla P} > 1.1\frac{1}{\nu_0 + \tau_0 m/\rho}\omega_{\max}^{\mathrm{Newt}} \right\rangle.$$

Figure 9 displays the evolution of $\mathcal{O}(\tilde{dp})$. The critical pressure $\tilde{dp}_c$ is then determined by the first significant jump of this quantity.

In order to determine the critical length λ_c from $\tilde{dp}_c$ we follow the argument of [3] and [6] for a pore network model, suggesting that the critical pressure has a simple geometrical meaning. Indeed, the critical pressure can be determined by finding the path which minimizes the sum of the pressure threshold $\Delta P = \min(\sum \delta p_c)$, where δp_c denotes the critical pressure of the links. In our context, the argument can be understood as follows. As we have seen in fig. 5, close to the pressure threshold, only one single chanel path remains flowing. This path can be approximated by a channel with variable opening $b(s)$. Assuming the lubrication approximation, one can then compute the flow rate along this channel using eq. (11)

$$Q = \frac{2b(s)^3}{3\rho\nu_0}\left(\frac{1}{\nabla P}\right)^2\left(\nabla P - \frac{\tau_0}{b(s)}\right)^2\left(\nabla P + \frac{\tau_0}{2b(s)}\right). \quad (30)$$

When Q tends to zero, because of mass conservation, it implies that the quantity $\nabla P - \frac{\tau_0}{b(s)}$ tends to zero all along the channel. The pressure gradient is thus known everywhere. Since the pressure drop is the integration of the gradient, we have then $\Delta P_c = \int \tau_0/b(s)\mathrm{d}s$. Consequently, the critical pressure drop can be computed by finding the path that minimizes the quantity:

$$\Delta P_c = \tau_0 \min_{\mathcal{C}}\int \frac{1}{b(s)}\mathrm{d}s, \quad (31)$$

where $\mathcal{C}$ denotes all the flow paths that connect the inlet to the outlet.

From the critical pressure drop, one can then define a critical length as

$$\lambda_c = \tau_0\frac{L_x}{\Delta P_c} = \frac{\lambda}{\tilde{dp}_c}. \quad (32)$$

This length represents thus the harmonic mean of the opening along the minimum path $\lambda_c = (1/L_x\int b^{-1}(s)\mathrm{d}s)^{-1}$ which is related to the "directed polymer problem" [34, 35].

Figure 7 displays the evolution of λ_c as a function of the porosity of the medium (and different realization). From the argument used previously, it is expected that the critical length increases with the porosity. Indeed, with the stochastic procedure used, the distance between solid regions increases necessarily with the porosity.

To summarize, eq. (29) can thus be rewritten as

$$q = \frac{K_{\mathrm{Darcy}}\tau_0}{\lambda\rho\nu_0}\mathcal{G}\left(\frac{\lambda\Delta P}{\tau_0 L_x} - \frac{\lambda}{\lambda_c(\phi)}\right), \quad (33)$$

$$\text{with} \quad \lim_{x\to\infty}\mathcal{H}(x) = x + O(x).$$

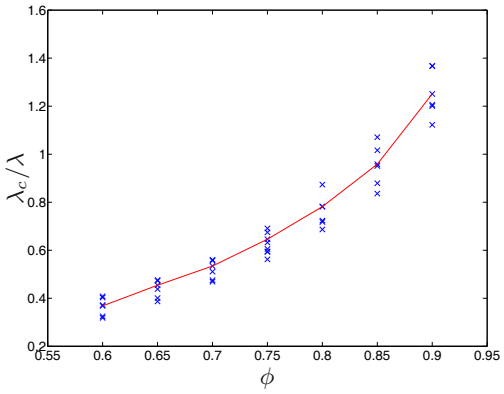

Fig. 7. Critical length λ_c as a function of the porosity. The crosses represent different realizations, the line represents the statistical average. The other parameters are $L_x = 512\ \delta x$, $\lambda = 6\ \delta x$, $m = 10^9$, $\Lambda = 0.2$, $\nu_0 = 10^{-3}$ and $\tau_0 = 10^{-5}$.

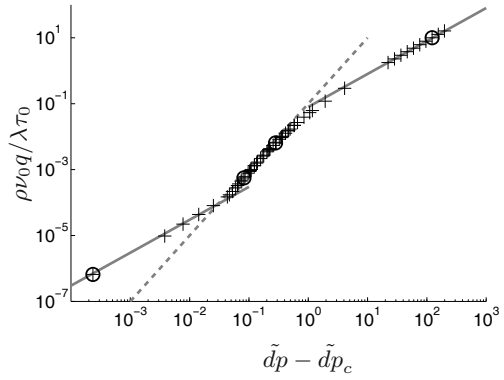

Fig. 8. Dimensionless flow rate $\rho\nu_0 q/\lambda\tau_0$ as a function of the nondimentional distance to the critical pressure $\tilde{dp} - \tilde{dp}_c$. The two plain lines have a slope of one and the dashed line has a slope of two. The four circles represent the corresponding simulations of fig. 5. The parameters are $\phi = 0.75$, $L_x = 1024\ \delta x$, $\lambda = 6\ \delta x$, $m = 10^9$, $\Lambda = 0.2$, $\nu_0 = 10^{-3}$ and $\tau_0 = 10^{-5}$.

3.3 Flow rate regimes

In this section, we thoroughly analyse the flow rate above the critical pressure $\tilde{dp}_c$. Below $\tilde{dp}_c$ the theoretical flow rate is zero. The numerical flow rate follows Darcy's law with a very high viscosity as we have already seen before.

On fig. 8, we have plotted the flow rate as a function of the distance to the critical pressure $\tilde{dp} - \tilde{dp}_c$. One can clearly observe three scaling regimes given by $q \propto (\tilde{dp} - \tilde{dp}_c)^\beta$. For small pressure differences β equals one (Regime I), then for a higher pressure difference we state $\beta = 2$ (Regime II), then by increasing the pressure β is equal to one again (Regime III). Remarkably, these three regimes are identical to those observed by Roux and Hermann [3] in a very idealized system. Indeed, they have used a regular resistance network model with uniformly distributed pressure thresholds. They have assumed an affine relationship between the voltage and the current, which is clearly not the case in the present work. Additionally, they noted that the exponent $\alpha = 2$ is independent of the threshold distribution. However, Roux and Hermann have also reported that this scaling regime changes by modifying the current-voltage relationship (linear to quadratic). It is therefore quite remarkable that we find a similar scaling despite the fact that we have a different geometry and a very different flow rate-pressure difference relationship inside each throat.

One should then recall the interpretation of Roux and Hermann for those three regimes.

Regime I corresponds to a single channel flow curve. Indeed, as we have already observed, just above the critical pressure only one single flow path is open. This implies that, for increasing pressure, as long as we do not open new pathes, one should then expect the flow rate to follow eq. (30). In the case of Roux *et al.*, this relationship was affine, leading to the exponent one. In the present case, the single channel should have two exponents. At very small pressure, one should have a quadratic behavior followed by a linear one. We think that the quadratic behavior is not seen due to numerical precisions since it involves very low flow rates. Moreover, the fact, that we do observe the linear behavior suggests that the first channel reaches its linear regime before new channels are opened in the media.

Regime II corresponds to the regime where an increase of pressure triggers an opening of new paths as depicted by fig. 5. The heuristic argument proposed by Roux and Hermann is the following. Assuming that in this regime, an infinitesimal increase of pressure $\mathrm{d}P$ leads to a proportionally increase of the number of new channels: $\mathrm{d}N \propto \mathrm{d}P$. A linear relationship between the flow rate and the pressure leads then to an exponent of two. Here also, the argument crucially depends on the linear flow rate curve assumption. It is thus remarkable that in the present work, we observe precisely the same coefficient. Additionally this result is consistent with the analytical result of Sinha and Hansen [25] which obtain a quadratic dependence using a mean field approach.

As expected, Regime III corresponds to the case where all the fluid is flowing and has a quasi-Newtonian behavior. In this case one retrieves the standard Darcy's law.

A qualitative confirmation of this argument can be observed on fig. 9, where we have plotted the ratio of opened fluid ($\mathcal{O}$) as a function of the distance to the critical pressure $\tilde{dp} - \tilde{dp}_c$. Regime I corresponds to a constant value of $\mathcal{O}(\tilde{dp} - \tilde{dp}_c)$. Regime II starts simultaneously with a significant increase of $\mathcal{O}$ and Regime III begins once $\mathcal{O}(\tilde{dp} - \tilde{dp}_c)$ reaches a plateau. Interestingly, we note that in Regime II, the curve is not completely smooth but displays at some point a step-like evolution that characterizes the opening of new channels (for instance at $\tilde{dp} - \tilde{dp}_c \simeq 8 \cdot 10^{-2}$ on fig. 9). We also remark that new channels do not necessarily connect the opposite borders of the porous medium, they might also branch from prexisiting ones. As the pressure increases, channels become more difficult to define. It therefore complicates the estimation of the increase of the number of open channels.

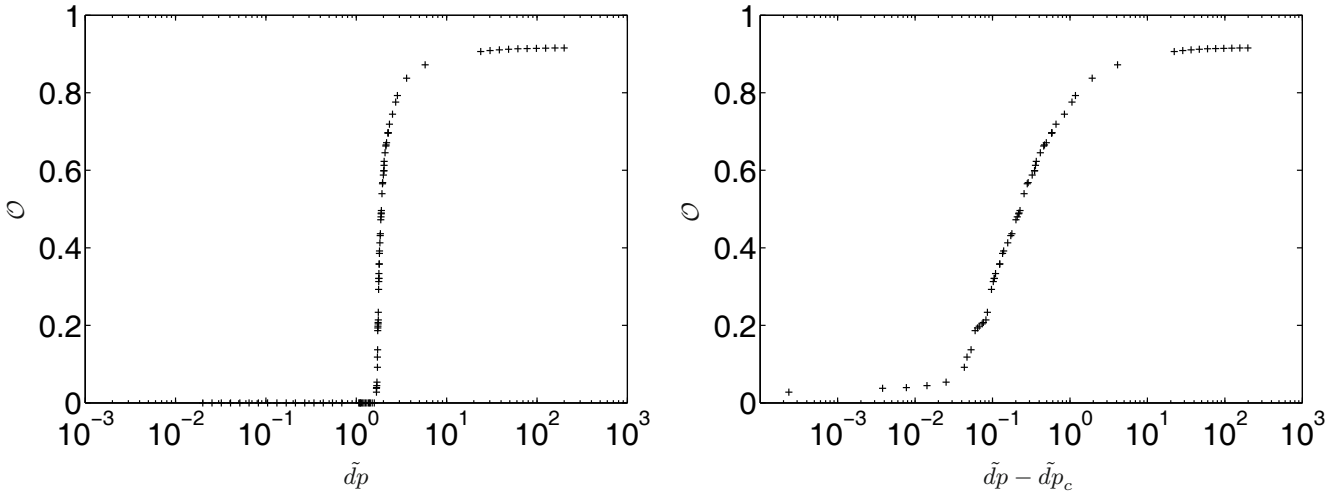

Fig. 9. Active proportion $\mathcal{O}$ as a function of the dimensionless pressure $\tilde{dp}$ and of the distance to the critical pressure $\tilde{dp} - \tilde{dp}_c$.

4 Conclusion

In this work, we have used a Lattice-Boltzmann scheme able to solve yield-stress fluid flow in porous media. We have analysed the different flow structures inside the media. Three different scaling regimes could be distinguished. Regime I that corresponds to the situation where fluid is flowing in only one channel. Here, the relation between flow rate and pressure drop is given by the non-Newtonian Poiseuille law. During Regime II an increase in pressure triggers the opening of new paths and the relation between flow rate and the difference in pressure to the critical yield pressure becomes quadratic: $q \propto (\tilde{dp} - \tilde{dp}_c)^2$. Finally, Regime III corresponds to the situation where all the fluid is sheared. In this case, we obtained $q \propto (\tilde{dp} - \tilde{dp}_c)$. It is interesting to note that most of the generalizations of Darcy's law that have been proposed (see eq. (26)) from experimental or numerical studies correspond only to the last regime.

In a recent article, Sinha and Hansen [25] proposed an analogy between two phase flow with the Bingham flow problem in porous media. The basic idea is that immiscible bubbles require a minimal pressure drop in order to go through pore throats. This threshold depends on the throat radius and the local saturation. Using a mean field approach, they derived analytically a quadratic dependence of the flow rate on the pressure. In recent simulation of blob dynamics in the same stochastic porous media, Yiotis *et al.* [32] demonstrated numerically such a scaling regime, which confirms the pertinence of this analogy. Further work will be dedicated to the study of two-phase flow or other rheological laws and boundary conditions (the effect of wall slippage particularly) in order to test the robustness of those regimes.

The authors would like to thank Alex Hansen and Irina Ginzburg for usefull discussions, the "Agence National de la Recherche" for financial support of the project LaboCothep ANR-12-MONU-0011 and the CCR of UPMC for computational resources.

References

1. G. Barenblatt, V. Entov, V. Ryzhik, *Theory of fluid flows through natural rocks* (Norwell, MA (USA); Kluwer Academic Publishers, 1989).
2. W.R. Rossen, J. Colloid Interface Sci. **136**, 1 (1990).
3. S. Roux, H.J. Herrmann, Europhys. Lett. **4**, 1227 (1987).
4. C.B. Shah, Y.C. Yortsos, AIChE J. **41**, 1099 (1995).
5. M.T. Balhoff, K.E. Thompson, AIChE J. **50**, 3034 (2004).
6. M. Chen, W. Rossen, Y.C. Yortsos, Chem. Eng. Sci. **60**, 4183 (2005).
7. T. Sochi, M.J. Blunt, J. Petrol. Sci. Engin. **60**, 105 (2008).
8. T. Sochi, Polymer **51**, 5007 (2010).
9. M. Balhoff, D. Sanchez-Rivera, A. Kwok, Y. Mehmani, M. Prodanović, Transport Porous Media **93**, 363 (2012).
10. H. Park, M. Hawley, R. Blanks, SPE (11), 4722 (1973).
11. T. Al-Fariss, K.L. Pinder, Cana. J. Chem. Engin. **65**, 391 (1987).
12. G.G. Chase, P. Dachavijit, Sep. Sci. Technol. **38**, 745 (2003).
13. X. Clain, Ph.D. thesis, Université Paris-Est (2010).
14. D. Rothman, Geophysics **53**, 509 (1988).
15. S. Succi, E. Foti, F. Higuera, Europhys. Lett. **10**, 433 (1989).
16. Y. Qian, D. D'Humières, P. Lallemand, Europhys. Lett. **17**, 479 (1992).
17. L. Talon, J. Martin, N. Rakotomalala, D. Salin, Y. Yortsos, Water Resour. Res. **39**, 1135 (2003).
18. L. Talon, J. Martin, N. Rakotomalala, D. Salin, Y. Yortsos, Phys. Rev. E **69**, 066318 (2004).
19. L. Talon, D. Bauer, N. Gland, S. Youssef, H. Auradou, I. Ginzburg, Water Resour. Res. **48**, W04526 (2012).
20. E. Aharonov, D.H. Rothman, Geophys. Res. Lett. **20**, 679 (1993).
21. S. Gabbanelli, G. Drazer, J. Koplik, Phys. Rev. E **72**, 046312 (2005).
22. J. Psihogios, M. Kainourgiakis, A. Yiotis, A. Papaioannou, A. Stubos, Transport Porous Media **70**, 279 (2007).
23. A. Vikhansky, J. Non-Newtonian Fluid Mech. **155**, 95 (2008).
24. I. Ginzburg, K. Steiner, Philos. Trans. R. Soc. London, Ser. A **360**, 453 (2002).

25. S. Sinha, A. Hansen, EPL **99**, 44004 (2012).
26. T.C. Papanastasiou, J. Rheol. **31**, 385 (1987).
27. I. Ginzburg, J. Stat. Phys. **126**, 157 (2007).
28. I. Ginzburg, F. Verhaeghe, D. d'Humières, Commun. Comput. Phys. **3**, 427 (2008).
29. I. Ginzburg, Phys. Rev. E **77**, 066704 (2008).
30. D. d'Humières, I. Ginzburg, Comput. Math. Appl. **58**, 823 (2009).
31. C. Pan, L.S. Luo, C.T. Miller, Comput. Fluids **35**, 898 (2006).
32. A.G. Yiotis, L. Talon, D. Salin, Phys. Rev. E **87**, 033001 (2013).
33. T. Chevalier, C. Chevalier, X. Clain, J. Dupla, J. Canou, S. Rodts, P. Coussot, J. Non-Newtonian Fluid Mech. **195**, 57 (2013).
34. M. Kardar, Y.C. Zhang, Phys. Rev. Lett. **58**, 2087 (1987).
35. L. Talon, H. Auradou, M. Pessel, A. Hansen, EPL **103**, 30003 (2013).